JOURNAL OF AIRCRAFT
Vol. 55, No. 6, November–December 2018

Aeromechanics Analysis of a Hummingbird-Like Flapping Wing in Hover

David Coleman,* Kanika Gakhar,† and Moble Benedict‡
Texas A&M University, College Station, Texas 77843
and
Jason Tran§ and Jayant Siroh¶
University of Texas at Austin, Austin, Texas 78701

DOI: 10.2514/1.C034726

This paper presents an in-depth investigation into the instantaneous forces, flowfield, and wing deflections of a flapping wing used on a hover-capable robotic hummingbird. The goal was to understand the relationship between instantaneous lift and wing shape. An experimental rig was constructed, which flapped the wing at 20 Hz and measured instantaneous loads normal to the stroke plane. To separate inertial and aerodynamic loads, a novel approach was developed in which the wing spatial and temporal displacement was obtained using digital image correlation. From this, the instantaneous inertial force normal to the stroke plane was calculated based on mass distribution. The flowfield on the wing was resolved using particle image velocimetry, which revealed attached flow at steep angles of attack and several strong vortices. It was found that lift was sensitive to both unsteady aerodynamics and deflection. This study marks the first time that these quantities have been measured for a flapping wing used on a hover-capable vehicle, using a procedure developed for extracting pure aerodynamic force on a flexible structure. This effort has resulted in experimental data useful for validating high-fidelity flapping wing aeroelastic computational models.

I. Introduction

AMONG birds, bats, and insects, there are at least several hundred thousand species of living creatures on Earth that are capable of sustained and powered flight [1–3]. In contrast to human-made machines with propellers and rotors, biological creatures fly using reciprocating wings. Such wings are extraordinary and capable of large instantaneous force generation. They are structurally tuned for an optimal balance between chordwise flexibility and spanwise stiffness due to the presence of materials comparable to some of the most advanced ones today [4–6]. They are aeroelastically refined through carefully tailored flexibility, employing fluid-dynamic interactions and inherent inertial-elastic couplings to amplify aerodynamic forces [7–9]. This is especially true for hovering flight, in which the wings complete large sweeping motions, undergoing substantial torsion at the stroke ends and reversing pitch and camber for positive force production [10–12]. Although it has yet to be determined whether pitching is done actively with internal muscles or is the passive response to inertial-aerodynamic loading, studies have shown that the combination of these two forces alone is capable of generating all the pitching and cambering observed in hummingbird and insect wings [13–16]. This further underscores the need for proper aeroelastic tailoring.

For micro air vehicle (MAV) developers interested in hover-capable flapping-wing flight, it is critical to understand such aeromechanics and force production to design functional wings for a biomimetic robotic hummingbird as shown in Fig. 1 [17]. In spite of the existence of a few two-winged, hover-capable flapping wing MAVs, a detailed look at the lift production process on a vehicle that has successfully flown has not been conducted [18–20]. However, researchers have long recognized the need for developing flapping wings with high thrust-to-power and lift-to-drag ratios. Subsequently, there has been several experimental and computational force and flowfield investigations into the aeromechanics of various wing designs with the goal of discovering performance trends across wing designs. These studies can be divided generally into three categories.

A. Investigations with Natural Wings

These efforts have focused on characterizing structural properties of insect wings and flowfield characteristics associated with hummingbird wings. It has been found that structural deformation comes mainly from inertial loads in the stroke plane in Manduca Sexta. Additionally, the variation in spanwise and chordwise structural stiffness, which depend on wing venation and size, has been tabulated for a variety of species [21–24]. Flowfield studies on hummingbird wings have shown attached flow at very high angles of attack, and the presence of leading edge vortices as well as increased L/D for larger-aspect-ratio wings [25,26]. Throughout these studies, biological wings repeatedly outperform the best microscale wings and rotors designed today.

B. Studies with Arbitrarily Designed, Nonflying Wings

Because of the difficulties of developing a flying flapping-wing vehicle and associated flight-capable wings, the majority of aeromechanical studies investigate biologically inspired, yet arbitrary wing designs that vary significantly across experiments. A few of these studies are based on dynamically scaled insect wings flapped in a thick, viscous fluid [27–29]. From these, force and particle image velocimetry (PIV) measurements have shown the presence of aerodynamic structures on flexible wings analogous to rigid wings, including added mass and rotational lift. Additionally, these studies have shown that excessive wing flexibility (due to no cross member support) is detrimental to lift production. The rest of the experimental studies have focused on flexible flapping wings in air of arbitrary designs, aimed at replicating characteristics of biological wings such as planform shape, mass, or aspect ratio [29–34]. Most of these studies are concerned with quantifying wing performance with small design changes. Although

Received 1 September 2017; revision received 18 March 2018; accepted for publication 15 April 2018; published online 2 August 2018.

*Graduate Research Assistant, Department of Aerospace Engineering, 701 H R Bright.
†Undergraduate Research Assistant, Department of Aerospace Engineering, 701 H R Bright.
‡Assistant Professor, Department of Aerospace Engineering, 701 H R Bright.
§Graduate Research Assistant, Aerospace Engineering and Engineering Mechanics.
¶Assistant Professor, Aerospace Engineering and Engineering Mechanics.

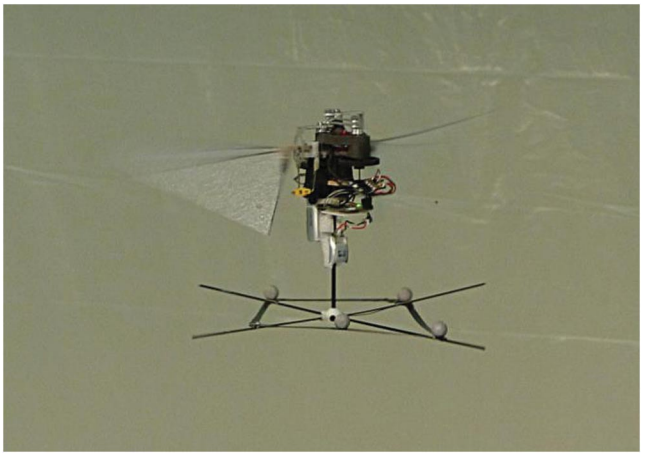

Fig. 1 Two-winged hover-capable robotic hummingbird during controlled flight (Ref. [17]).

these designs are not validated on a flying system, some interesting phenomena associated with varying stiffness and structural design have been discovered nonetheless. A stiff leading edge and linear spanwise twist simultaneously increase thrust and decrease power requirements, while an overly flexible wing sheds more vortices during each half stroke, contributing to a loss of lift. Computational studies have used computational fluid dynamics solvers, analytical models, surrogate models, and panel methods in order to simulate the flowfield and structural deflection of model insect wings [30,35–38]. Validation with extensive experimental data is what is needed for these high-fidelity computational models. Thus, while many nonflying flexible flapping wings have been developed, it is uncertain whether such designs would be workable on a real system.

C. Experiments with Wings Used on Flying Vehicles

These studies represent a minority of the investigations of flexible flapping wings, but provide relevant experimental data and hold the most insight. Most are concerned with characterizing forces, flowfield, and performance of wings for forward-flying ornithopters, hence not directly addressing the aeromechanics of hovering flight [4,39]. Some aspects of hovering aeromechanics have been investigated and addressed in Ref. [40], one of the first of such endeavors. In this study, time-averaged forces of a flight-capable, hovering, flapping wing were quantified, and length, aspect ratio, camber, shape, and chord distribution were varied to minimize input power and maximize thrust. The final wing design was very similar in form to hummingbird wings and was used on the flying vehicle.

What is of interest, however, in the analysis of flapping wing force production is the time history of the pure instantaneous aerodynamic forces. Extracting these from the force measurements is challenging because inertial forces normal to the stroke plane (termed "normal inertial forces" hereafter) are measured along with the aerodynamic forces, thus contaminating pure instantaneous aerodynamic force measurements. Therefore, a proper characterization of wing performance and comparison across multiple designs is not possible without eliminating inertial force. This problem has been addressed by flapping the wing in a vacuum chamber where only inertial forces are present, or replacing the wing with a fixed point mass having negligible aerodynamic forces, or calculating it analytically [4,31,35,41].

Each of these methods, however, investigates only inertial forces in the stroke plane, and even disagrees over the relative magnitude of the aero and inertial forces [42–44]. Thus normal inertial forces due to the upward motion of the flexible wing have not been considered. Although studies have addressed the vertical movement of the wing C.G. for a rigid wing during pitching [28], the significance of normal inertial loads of a flexible wing needs to be quantified. The traditional method of flapping the wing in a vacuum chamber and subtracting the inertial force from the total force measured in air is not possible for flexible wings because the structural dynamics of a flexible wing in air and vacuum will be different. In fact, there will be no normal inertial loads because motion normal to the stroke plane, which is only due to aerodynamic force, will be absent in a vacuum. Likewise, horizontal loads could also be different. Therefore, a new method must be developed for extracting any inertial loads from a flexible flapping wing.

This study uses a novel idea in which the wing deflection measurements obtained using digital image correlation (DIC) are used to quantify normal inertial forces. By subdividing the wing into a series of grid point elements with finite mass properties and measuring the displacement of each of the grid points at discrete flap times, the acceleration of each wing mass element is reconstructed. This result is then used to calculate the instantaneous inertial loads. The computed inertial forces can be subtracted from the total force to get the pure aerodynamic force. Additionally, the wing deflection measurements also bridge the gap between the force and aerodynamic flowfield measurements, because the aerodynamics are strongly affected by the passive wing shape.

DIC techniques have been previously used on a series of arbitrarily designed flexible flapping wings in hover to understand the effect that leading edge bending and pitch angle at the 83% span have on force production, and also for quantifying the influence that variations in wing flexibility have on structural deflection and flowfield [32,45]. Additional experiments on rectangular planform flexible wings have measured quarter and midspan deflections. These were provided as an input to an analytical aerodynamic model that showed good agreement and demonstrated the use of experimental data for model validation [46]. While providing insights into flexible wing design, these studies are based on arbitrary wing designs unproven on a flying system. Thus, in the interest of understanding the aeromechanics of hummingbird-like flight, these are not choice wings. For instance, the wings used in [32,45] experiments only duplicated the mass and planform shape of hummingbird wings. Characteristics such as the distribution of mass and wing structure, which are significantly important because these affect the final wing deflected shape, were not considered. A key wing structural element, for example, of avian wings, is the angle of the feather quills relative to the forearm of the bird, which is known to strongly influence the wing's torsional qualities [47,48]. Angled battens on flexible flapping wings replicate these structural qualities; however, the wing battens in Refs. [32,45] were perpendicular to the leading edge, resulting in even greater differences between experimental and biological wings. Thus quantitative shape of biomimetic wings used on a flying robotic hummingbird is what is missing. Measuring these has the potential to expand our understanding of flexible flapping wing design, and understand whether wing displacement is largely due to fluid-dynamic or inertial-elastic forces [21,22,35,45].

The purpose of this paper, therefore, is threefold. First, it is to quantify the instantaneous lift forces of a flexible hover-capable robotic hummingbird wing flapping at 20 Hz (operating frequency in hover), and present a new experimental methodology for removing inertial forces from the wing force measurements. Second, it is to quantify the instantaneous shape of the wing in terms of key parameters such as pitch angle, twist distribution, and camber. And third, it is to measure the flowfield using PIV to characterize the fluid-structural interactions directly on the surface of the wing during flapping at operational frequency. Because each of these components is so strongly interlaced, a proper analysis of the wing aeromechanics would not be complete without all three. This paper presents the details of each of these experiments and an in-depth discussion of the final aeromechanical analysis of the results.

II. Experimental Methodology

The purpose of these experiments was to quantify the time history of pure aerodynamic lift, wing deflection, and flowfield of the wing used on our hover-capable robotic hummingbird MAV in hovering flight at the operational frequency of 20 Hz using active flapping and passive aeroelastic pitching as seen in natural flyers. Because of significant size, weight, and structural constraints, it was not possible to measure these while the wing is flapping on the vehicle. Therefore,

an experiment was developed that faithfully reproduced the flapping kinematics and thus duplicated the rigid and flexible body dynamics of the wing and the associated flowfield features.

For this experiment, first a duplicate of the robotic hummingbird wing was manufactured using the standard process for making wings for the robotic hummingbird. It has been shown previously that the wings produced by the current manufacturing technique perform very consistently. At 20 Hz, the lift produced by each of a series of six wings varied only by ±2.5% of the mean lift of all the wings. In terms of performance, the wing is thus an accurate duplication of that used on the vehicle [17]. Next, an accompanying experimental rig was constructed using high-precision (±0.0001″) machined linkages of the same geometry as those used on the vehicle that generated the same flapping kinematics [17]. Shown in Fig. 2 is 50 cycles of flap angle kinematics overlaid demonstrating the consistency and repeatability of the kinematics. Note that the amplitude of the stroke is ±55°, which is the same as that measured directly on the vehicle. Additionally, in the event of a mechanical failure during vehicle flight testing, replacing broken linkages with new ones machined identically does not result in a change in vehicle flight. This means that the wing kinematics do not vary with copies of the mechanical linkages. Thus the flapping kinematics are identically reproduced on the experimental rig, resulting in the same wing motion. On the experimental rig (Fig. 3), the drive motor shaft torque was measured with a torque cell, flap angle was measured using a shaft encoder, a beam load cell measured wing force normal to the stroke plane, and a shunt resistor measured current. All data were sampled at 2000 Hz, collected via National Instruments data acquisition devices, and recorded with a LabVIEW program.

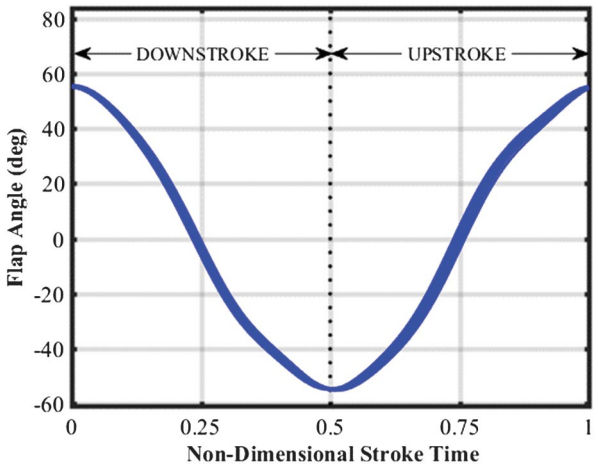

Fig. 2 Flap angle kinematics for hover-capable robotic hummingbird duplicated on bench-top experimental rig.

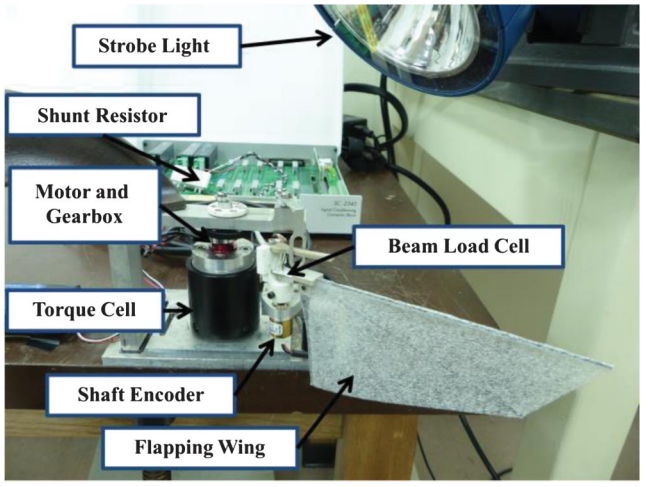

Fig. 3 Experimental bench-top rig for instantaneous force measurements.

For these experiments, only a single duplicate wing was incorporated into the setup, because there is no expected interactions if two wings were present. This was because, of all the unsteady aerodynamic forces acting on a flapping wing, the only one resulting from wing-wing interaction is "clap-and-fling" (or "clap-and-peel") [49]. When clap-and-fling mechanisms are present, the aerodynamics and flowfield of the wings affect each other. However, this phenomenon, which can influence force production over the entire stroke, occurs only when the smallest flap angle between the wings (which happens at the stroke ends) is at most 20° [50]. For the current robotic hummingbird, the closest the wings approach is 70°, far outside the range in which the wing aerodynamics would change due to the presence of a mirror wing. Therefore, the single flapping wing aerodynamics will be identical to those measured on the same wing but with a pair of wings flapping together, which is the case on the flying system.

Because wing deflection and thus aerodynamic force and flowfield are intrinsically a function of the wing design, an overview of the specific design elements and structural components is in order here, with more details in Ref. [17]. Each component design and material selection is critical to developing a wing with the highest strength-to-weight ratio to both reduce and withstand high inertial loading during flapping. Additionally, the requirement was to generate lift equal to half the vehicle weight at 20 Hz, because higher flapping frequencies generate prohibitively high vibratory loads. Figure 4 shows a schematic of the wing with some components labeled. It has a stiff leading edge carbon fiber rod 1 mm in diameter, so chosen to minimize bending in and normal to the flapping plane, because these reduce the overall lift of the wing. Additionally, the wing features a stiff root spar (1 mm carbon fiber rod) attached via a structurally tuned flexible carbon fiber shim to the wing root, not unlike a flexbeam found in a traditional helicopter rotor blade. The purpose of this shim is to function as a torsional spring, allowing the root spar to rotate, and permitting the inboard portions of the wing to operate at a steep angle of attack, instead of being perpendicular to the tangential velocity. The flexible root shim in bending is illustrated in Fig. 4. Incorporating this substantially increased the lift. The wing fabric is a flexible foam membrane glued to this carbon fiber frame, which generates low acoustic signature and generates a smooth curvature of the wing during flapping. A free-floating cross spar is then glued to the foam membrane, which improves the wing shape during flapping and enhances lift. The wing mass, planform shape, dimensions, and material distribution are shown graphically in Fig. 5.

A. Wing Deflection Methodology

To quantify the deflection of flexible flapping wings, previous researchers have employed various techniques. These include creating a specialized MATLAB program for tracking a set of three points on hawkmoth manduca sexta wings, or extracting wing shape and pitch angle from PIV measurements [21,44]. Unfortunately, these techniques provide displacements only at a few discrete wing locations. A large distribution of points and corresponding displacements at high spatial and temporal resolution are necessary for obtaining the deflected wing shape at different instances of flap for inertial force quantification.

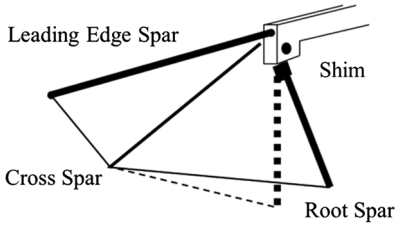

Fig. 4 Wing schematic. Flexible shim is shown in bent configuration. Foam membrane is stretched over spars.

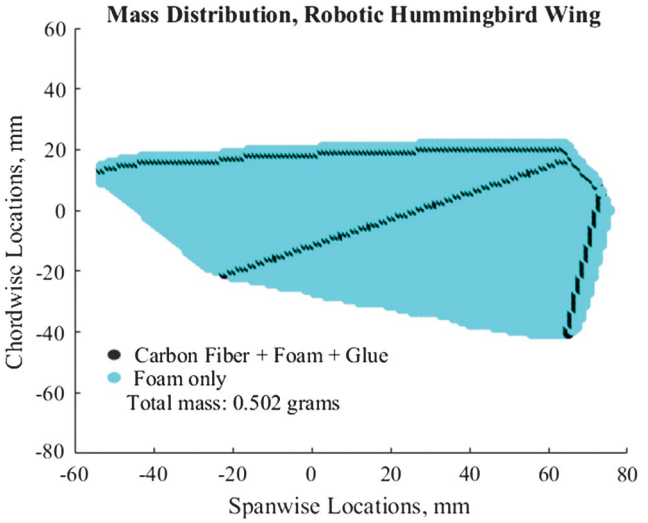

Fig. 5 Wing planform, structural components, and mass distribution of grid points.

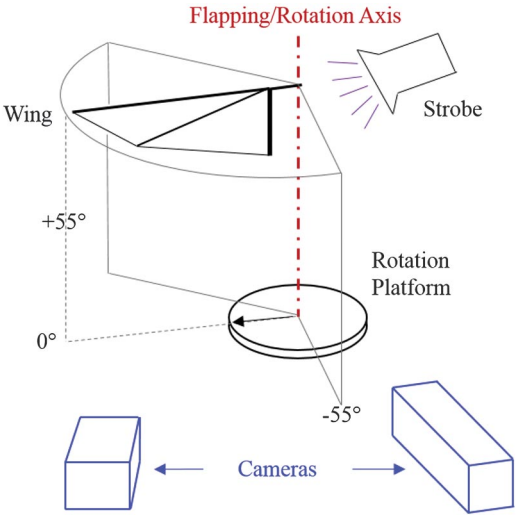

Fig. 7 Schematic of DIC experimental rig.

Digital image correlation (DIC) is an optical measurement technique that calculates the displacement of structural surface features by performing cross-correlations on two images taken at different loading conditions. It is a well-established technique that has previously been applied to flapping wings to measure deflections at various locations on the wing [32,45,46]. While these experiments quantified deflection of arbitrary wing design, they nevertheless demonstrated quantitatively the variation in force generation with wing flexibility and design. Additionally, they showed how first-order aerodynamic models using the measured displacement can give rough time histories of forces for simple wing geometries. The DIC experimental methodology involves 1) speckling of the wing with random black spots over a thin coat of white paint to create high-contrast visual features on the wing (Fig. 6); 2) angle indexing of the flapping wing apparatus for interrogation at the desired flap angles; 3) positioning and calibrating the cameras; 4) camera and strobe light trigger synchronization; 5) acquiring reference images of the wing in the undeflected configuration; and 6) vector field calculation from deformed images. Note that force measurements were taken with the wing flapping at 20 Hz after having been painted for DIC experiments. The values for the average lift generated throughout the flap cycle agreed with those presented in Ref. [17] within the expected error. For this reason, it is reasonable to conclude that the addition of a coat of paint did not substantially affect the mass distribution or elastic properties of the wing and that the measured displacement is therefore the same as that of the wings used in flight.

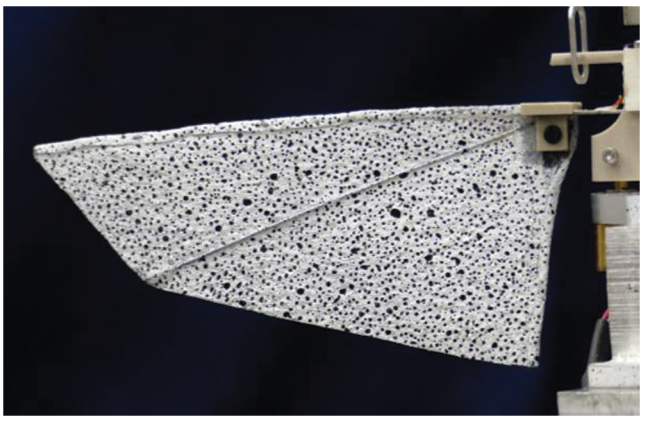

Fig. 6 Speckled wing prepared for DIC measurements.

One challenge in applying DIC to flapping wing experiments is that the wing's rigid body flapping motion and deflection moves it out of the camera field of view. To address the issue of rigid body motion, the entire experimental apparatus is mounted onto a rotation platform having a rotation axis concentric with the flapping axis as shown schematically in Fig. 7. The wing flaps from $+55°$ through the midstroke at $0°$ to $-55°$. Displacements are captured when the wing passes though the camera interrogation plane denoted by the dotted lines. The wing sweep volume can be rotated about the flapping/rotation axis, which rotates the wing's reference frame relative to the camera's reference frame, allowing the cameras to acquire the wing displacements at different selected angles within the stroke. The concentric rotation axes prevent introducing rigid body translation when indexing angles.

Because the current study involves an application of DIC to a flapping wing undergoing extremely large deflections with small cycle-to-cycle variations, there are a few additional challenges that had to be addressed. First, because of the extremely large wing deflections, the cameras had to be positioned such that their viewing angles are optimized for either when the wing deflects toward the camera (upstroke), or away from the camera (downstroke). Thus two different camera positions were used and calibrated. Additionally, the camera depth of field was maximized for large displacements using the smallest aperture possible and centered between the undeflected wing and the wing at maximum deflection. This resulted in images that remained focused even with large wing deflections. Second, the DIC algorithm failed to converge on a displacement field solution at 20 Hz, again as a result of substantial deflections. To address this, images are taken of the wing deflections at rest, 13 Hz, and 17 Hz. The displacement calculations are then performed in stepwise fashion from the reference to 20 Hz. The displacement vectors between each case are then added to obtain the final deflection.

Stroboscopic imaging was selected as the method of capturing images as it achieved a 10-bit intensity range in the captured images. Two Phantom Miro 310 cameras with 12-bit intensity depth and 1280×800 pixel resolution are used for the imaging with 50 mm lenses with aperture set at $f/11$. Although the cameras are capable of high-speed imaging, the short exposure times required to reduce motion blur did not allow for sufficient bit intensity contrast. The triggering system for stroboscopic imaging included the experimental rig flap angle shaft encoder, an NI data acquisition unit (DAQ), a programmable timing unit (for cameras), and a xenon strobe (10–40 μs flash duration). The shaft encoder measures the flap angle and is read by an analog programmable function input of the DAQ, which is then programmed to trigger at the desired encoder voltage level with either a falling (upstroke) or rising (downstroke) slope. Once triggered, the DAQ sends a pulse to the programmable timing unit to trigger the

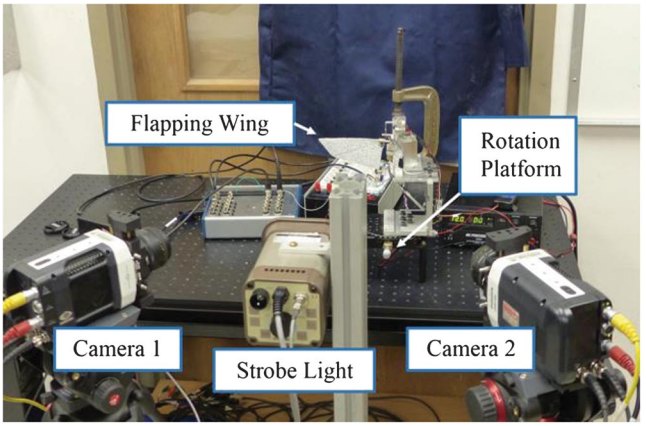

Fig. 8 Digital image correlation experimental setup, showing wing, rotating platform, cameras, and strobe light.

camera shutter, and then a second pulse 50 μs later to the strobe. The camera shutter is left open for 100 μs so that the entire strobe duration is captured. The resulting images show no motion blur and have excellent intensity contrast. Figure 8 shows the complete experimental setup, adapted for DIC measurements.

For the final measurements, a set of undeflected stereoscopic wing images was used as the reference image. The wing was then flapped at 13, 17, and 20 Hz and deflection measurements were made at each of these frequencies at flap angle locations that varied from the minimum flap angle to the maximum in increments of 10° (+55° to −55° in Fig. 7). Because the goal of the present study is to reconstruct the acceleration of the wing mass as accurately as possible and because the motion may be nonlinear, the sequence of images from the experiments was visually inspected. If there were any two flap angles that showed greater than 20 mm of wing tip deflection between their respective images at 20 Hz, more images were taken at intermediate flap angles in order to generate a finer resolution of the wing motion. To address the issue of cycle-to-cycle flapping variations, 50 images are taken at each flap angle location so that the results can be averaged. The DIC postprocessing of the images was performed using LaVision StrainMaster [51]. Interrogation windows 39×39 were chosen because larger windows resulted in missing gird points along the wing edges, and smaller windows resulted in missing points within the grid due to too few correlation points. The images are processed using a step size of 8 pixels, which results in a displacement field resolution of 1.37 mm.

Once the deflection measurements are processed, the instantaneous normal inertial force could be calculated. For this purpose, a series of MATLAB postprocessing functions were written to extract the inertial force from the DIC displacement data. An overview of the steps employed is presented here in order to describe the procedure such that it can be repeated with other flexible flapping wing designs and structures.

1) *Refine reference grid*: As a result of the DIC postprocessing, a surface grid and associated displacements have been defined for the wing; however, there is a grid associated with the reference image of each flap angle, and each one of these is slightly different. Additionally, due to software limitations, some grid points along the edges of the wing may be lost. This is addressed by first comparing the reference grid to the reference images, and manually adding or removing grid points to completely and only cover the wing surface such that it is properly and fully defined. This procedure is first done for the reference images of all flap angles.

2) *Align and generate new grid*: To accurately calculate the inertial force, the wing displacements of all flap angles must be measured relative to the same initial position. Because there will be slight variations in the reference grids due to camera repositioning or calibration, it is necessary to align and scale the reference grids of each flap angle to be identical. This is done by selecting two specifically chosen spots from the speckled wing pattern, identifying the corresponding grid point locations on the reference grids of each flap angle, and aligning and scaling each to match the first reference image. With all reference grids scaled and realigned accordingly, a final grid is created, which overlays all reference grids and will be used as a master reference for all flap angles. At this point, the number of final grid points can be chosen, which for this case was selected to be about 5000. This is now the new reference grid for all future calculations (Fig. 5).

3) *Create spatial displacement surfaces*: Having generated a final reference grid to be used for all flap angles, it is now necessary to implement a surface interpolation of the DIC displacement data so that the deformed shape of the wing at each flap angle will be described in terms of the new grid. This was a simple matter of using MATLAB's built-in griddata function. For this interpolation, the "v4" setting was used because it does not require nonzero end points to account for the cases in which the final grid extends slightly beyond the edges of the reference grid for a given flap angle.

4) *Interpolate flap angle displacements*: The purpose of the proceeding steps has been simply to describe the displacement of the wing at each flap angle location with the same number of grid points relative to the same position. Having this now allows interpolation of the displacement data between measurements to the desired resolution. Additionally, at this step the stroke times at the flap angles with measured displacements are extracted from the time data collected during experimentation. This way, the interpolated displacements can be described in terms of stroke time rather than flap angle for differentiation.

5) *Differentiate displacement data*: Having wing displacements as a function of time to the desired temporal resolution, the smoothed derivative of each displacement point is calculated by differentiating a local quadratic least-squares fit to the set of displacement points that consists of the displacement point and four points prior in the time series and four points in the future. This gives a relatively continuous acceleration as a function of time for each grid point.

6) *Generate instantaneous inertial force*: Having acceleration as a function of time for all grid points, the acceleration time history of each grid point is multiplied by its representative elemental mass. The time history of the inertial force for each subelemental mass is the negative of this result, because inertial force is in the opposite direction of acceleration. Finally, summing the time histories of the inertial forces for each elemental mass results in the total inertial force for the wing as a function of time.

Figure 5 shows the final grid and associated masses of the wing based on the material selected and construction. For the carbon fiber spars, adhesive, and foam membrane, the density was experimentally derived and provided as an input for calculating the mass at each grid point. The total of all subelemental masses added together results in the total wing mass, which from the calculation is 0.5 g. The measured mass of the wing is 0.6 g, which includes the flexible carbon fiber shim located at the top right corner of the wing. The weight of the shim is approximately 0.1 g. As can be seen from Fig. 5, this region of the wing, and thus the flexible shim is not included in the mass element grid, and therefore is not accounted for in the mass calculation. As there may be slight differences between the measured and calculated wing masses, emphasis is placed on the development of a new experimental and analytical technique for extracting pure aerodynamic forces on a flexible structure with known mass distribution.

B. Flowfield Methodology

In addition to the force and deformation measurements, the flowfield during flapping in the immediate vicinity of the wing was quantified to identify salient aerodynamic features. A series of chordwise PIV experiments were conducted while flapping the wing at 20 Hz. The principle of PIV experimentation is to seed the volume of air through which the wing flaps with submicron smoke particles, illuminate a 2D plane intersecting the wing with a pulsed laser light source, and capture two consecutive frames with a known time delay between them using a camera perpendicular to the laser sheet. A software algorithm tracks the particles between frames and

establishes a velocity field based on the displacement between images.

PIV has been successfully conducted on rigid and flexible flapping wings in hover, as well as on hummingbird wings [25,26,28,32–34,38,45,50,52–57]. Most of these experiments were aimed at revealing gross structures in the surrounding flowfield, or investigating the flow in the wake of flapping wings. Only a few studies investigated flowfield in close proximity to the wing surface, and these affirmed the presence of attached leading edge vortices on hummingbird wings at high angles of attack [25,50,52–55]. Thus the effort of this study is to resolve detailed flowfield features on the surfaces of the flexible biomimetic wing and relate these to wing deflection.

The laser used was a dual-pulsed Nd:YAG laser with a 532 nm wavelength output and a maximum output power of 205 mJ. The camera was a Nikon Imager sCMOS with a 50 mm focal length objective lens. Because it was possible that 3-D effects might be present in the aerodynamics, the aperture was set to $f/1.8$ to get the narrowest focal plane so that any particles with significant out-of-plane motion would pass out of the laser, leaving only those particles with mostly in-plane translation. Triggering was done via the flap angle shaft encoder signal, which was converted from the approximately sinusoidal signal from the flapping motion to a square wave via a NAND gate. The programmable timing unit sent a trigger pulse to the laser and cameras on the rising edge of the square wave. To minimize reflections from the laser, the wing and experimental rig were painted flat black. Because it was shown previously for the DIC experiments that a coat of light paint on the wing does not affect the forces generated and thus the displacement, it is expected that the aerodynamic features measured by these PIV experiments are the same as those on the unpainted wings. Additionally, a mirror was placed on the opposite side of the wing as the laser in order to reflect the laser beam back and illuminate particles within the area cast by the shadow of the wing. The setup for PIV measurements is shown in Fig. 9.

The chordwise velocity field measurements were conducted with the experimental rig mounted to a rotating platform similar to the one used for the DIC measurements. With the flapping axis concentric with the platform rotation axis, the flapping stroke could be repositioned relative to the fixed laser plane and camera such that the flowfield was captured at different flap angles (Fig. 10). This technique is known as phase-locked PIV. For this study, two chordwise experiments were conducted. For the first, the wing was flapped at 20 Hz and interrogated by the laser sheet at the 70% spanwise location (shown in Fig. 10). The 2D flowfield was captured from the beginning of the downstroke to the end in flap angle increments of 10°. For the second chordwise study, the laser sheet

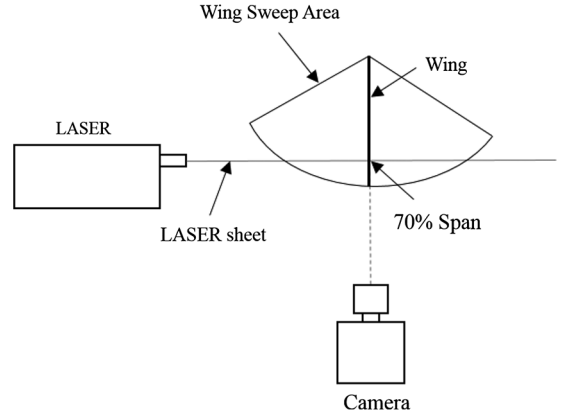

Fig. 10 Camera and LASER position for chordwise flowfield experiments, top-down view.

was moved to the 50 and 30% spanwise locations, the wing flapped at 20 Hz, and the flowfield was captured at the midposition of the dowstroke ($t/T = 0.24$ s), positive 30° of flap rotation ($t/T = 0.15$ s), and negative 30° of flap rotation ($t/T = 0.35$ s). These flap angles were chosen because the results from the first chordwise tests showed a clear difference in the flowfield for the two flap locations. As with the DIC measurements, 50 images were captured at each flap angle, and images that deviated significantly from the mean were discarded. The remaining ones were averaged to obtain a final velocity distribution at each flap angle.

III. Results and Discussion

For the instantaneous force measurements, experiments were conducted at 12.5, 15, 17.5, and 20 Hz with a flapping amplitude of 110°. The data were filtered at 100 Hz, and the results are plotted in Fig. 11. The first half of the plot shows the time history of the total force measured at the root of the wing during the downstroke, and the second half during the upstroke. A double peak in the vertical force occurs during both upstroke and downstroke, indicating slight changes in forces that may be due to variations in the wing shape caused by unsteady vortices or inertial loads. Although the general trend is similar across frequencies, the amplitude consistently increases with frequency. The stroke averaged forces are provided in the figure for each of the flapping frequencies, which agree well with time-averaged lift measured during the development of this wing [17]. These

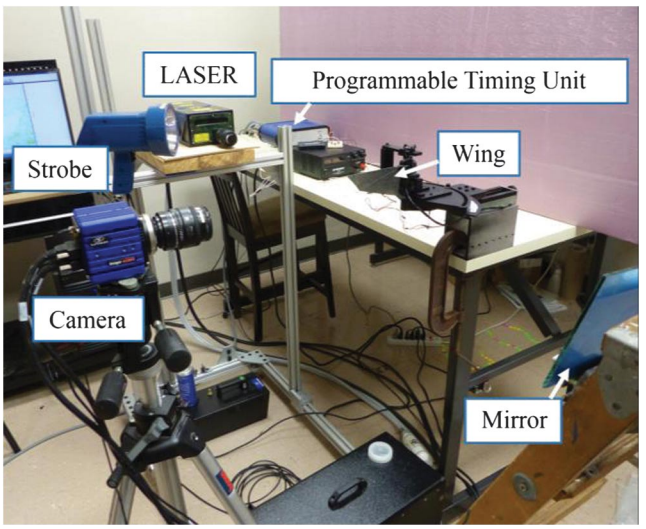

Fig. 9 Particle image velocimetry experimental setup showing key components, including wing, laser, and camera.

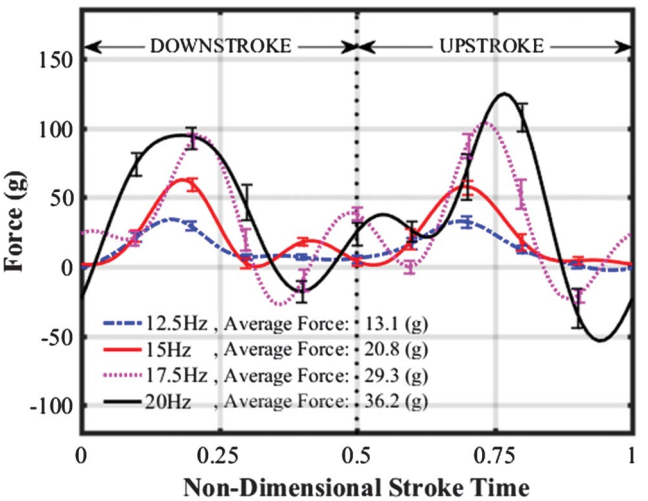

Fig. 11 Instantaneous force normal to flapping plane during stroke for range of frequencies.

instantaneous force measurements are critical in understanding how flowfield features and wing deflection affect the thrust production. Future experiments will be focused on determining the span and chordwise distribution of force and the location of the aerodynamic center (AC). This can be used to quantify the rolling and pitching moments generated during flapping as well as the controllability of the vehicle in flight.

There are yet two issues to address with regard to these measurements of forces normal to the flapping plane. First, for this flexible wing, it is quite evident from qualitative strobe light experiments that the deflection of the leading edge spar and displacement of the wing membrane are on the order of several millimeters. This is particularly true at the stroke ends where inertial loads are the highest, and at the midstroke where aerodynamic loads are highest. Thus, the above force measurements are contaminated by the normal inertial loads and must be removed. Additionally, the presence of a double peak in the force during both the upstroke and downstroke warrants further investigation in order to explain.

For these purposes, DIC measurements were taken of the wing during flapping at 20 Hz, which quantified the wing deflection at selected stroke times, and from these the structural accelerations were extracted. The relative wing displacements at rest, 13 Hz, 17 Hz, and 20 Hz are shown in 2D graphs in Fig. 12, with the grid generated by the DIC software for displacement calculations superimposed on the wing surface and a color gradient scale of out-of-plane wing displacements on the left. These results demonstrate the significant variation in wing displacement with frequency and the successful capture of complex, high-resolution wing shapes. At rest (0 Hz), there is no displacement, and the wing is orthogonal to the camera, hence the solid color of the wing. As the frequency increases, so does twisting and bending along the span, generating the color gradient from root to tip. At the tip, the deflection from initial position is the greatest, approaching 50 mm (2 in.).

To generate the most accurate measurements of wing displacement as possible, the experiments were phase-locked measurements, in which 50 measurements of the wing displacement were taken at each flap angle. The results were then averaged for a final displacement at each flap angle. Figure 13 shows a set of vertical displacement measurements during the midstroke across 50 flap cycles for three different points on the wing: one near the root, one at midspan, and one at the tip. The purpose of this figure is to quantify the representative error in the raw displacement measurements of the wing at midstroke. The mean and standard deviation are provided also. Although there are over 5000 more grid points at this flap angle with an associated statistical error, the results shown in Fig. 13 are quite representative of the data. A link to a video that replays the measured displacement field at all the flap angles is provided in Ref. [58].

Having high-resolution displacements for the wing at discrete flap angles, the time history of the inertial forces was calculated from the material assignment and time history of the acceleration of each of the subelemental grid points. The displacement of each of the wing subelements at discrete flap angle times was followed throughout the stroke, interpolated between measured flap angles, filtered, and differentiated twice as shown in Fig. 14. This displacement, velocity, and acceleration plot represents 60 cycles of wing kinematics of just one of the over 5000 wing grid points. The final instantaneous inertial force is the summation of each of the instantaneous acceleration time histories multiplied by their respective elemental masses. From the resulting nondimensional stroke time history of the inertial forces, the pure aerodynamic force was found by subtracting the calculated inertial force from the measured total force, which was obtained from overlaying and averaging 60 cycles of force data at 20 Hz. These results are plotted in Fig. 15, which shows the total measured force in black, the derived inertial force in blue, and the pure aerodynamic force in magenta. Interestingly, the prominent double peak in the total force data has been mitigated, especially in the upstroke, and thus this phenomenon appears inertial in nature. Although there is presently no computational analysis of the inertial forces against which to compare these results, they nonetheless make intuitive sense.

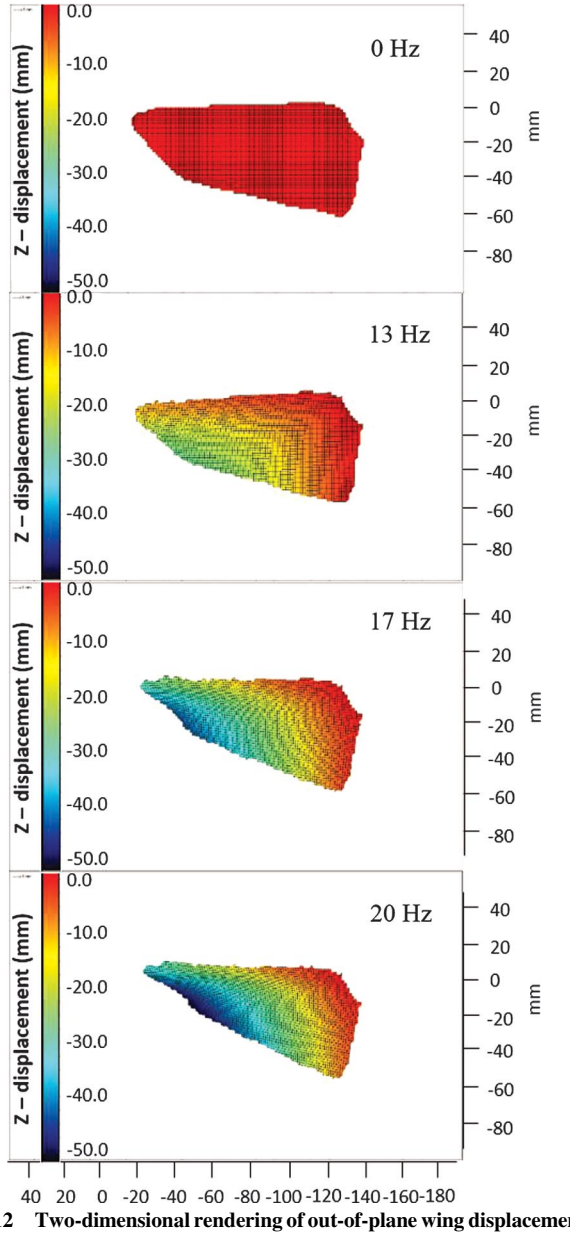

Fig. 12 Two-dimensional rendering of out-of-plane wing displacements with superimposed gridlines. Gridline intersections represent locations of subelemental masses.

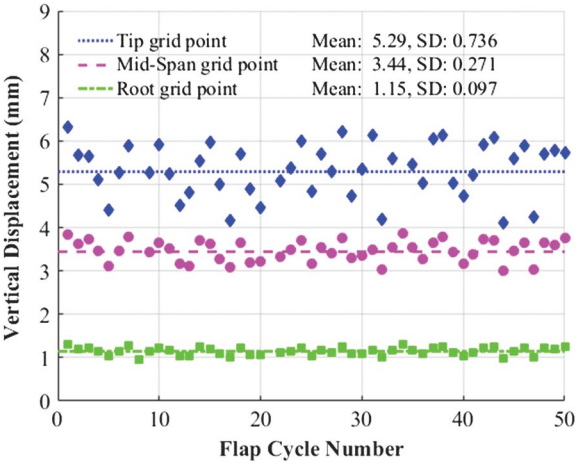

Fig. 13 Raw deflection measurements and statistical error of three representative wing grid points during midstroke.

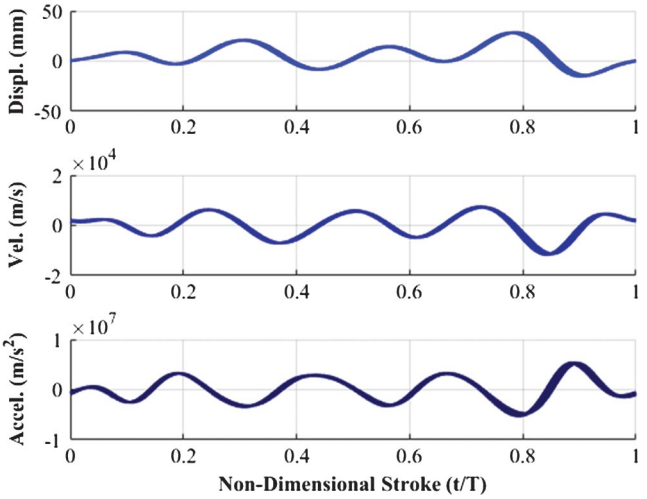

Fig. 14 Measured displacement from DIC experiments, and calculated velocity and acceleration of a single wing tip grid point.

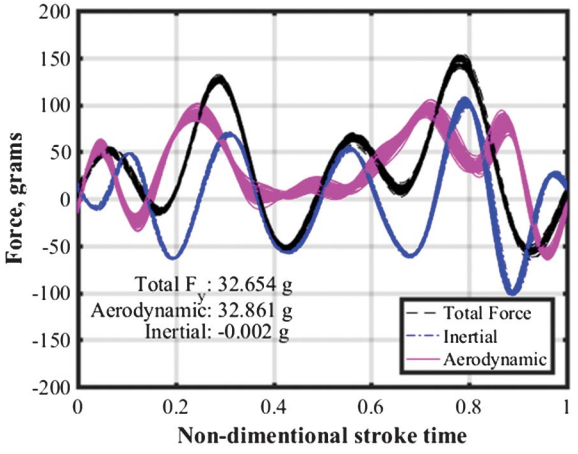

Fig. 15 Summary of vertical forces acting on the wing. Aerodynamic forces are equal to total minus inertial.

The inertial force calculation follows the general trend of the displacements: when the displacement of the wing is mostly in the positive direction during flapping, the inertial force is negative, and vice versa. Additionally, when summed over the entire flap cycle, the inertial force is zero, as expected.

Having established a new method for inertial force separation for a flexible structure with known mass distribution using measured displacements, it is possible to more fully characterize the influence of structural deformation on wing aerodynamics and aeromechanical interaction. Thus a presentation and discussion of the displacement and flowfield results follows, aimed at explaining some of the trends in the force data more carefully.

A. Wing Deflection Analysis

The pitch angle and camber are the two quantities obtained from DIC experiments that are useful in determining the deflected shape of the wing and gaining insight into the effect of wing shape on aerodynamics. These are illustrated schematically in Fig. 16 as seen from a cross sectional view perpendicular to the undeformed leading edge spar. Camber is a percentage, defined as the maximum distance between the straight line running from leading to trailing edge and the wing's curved shape, normalized by the wing chord. Further, the variation during flapping of these two parameters at the 70% spanwise location is shown in Fig. 17. A detailed examination of these two quantities follows.

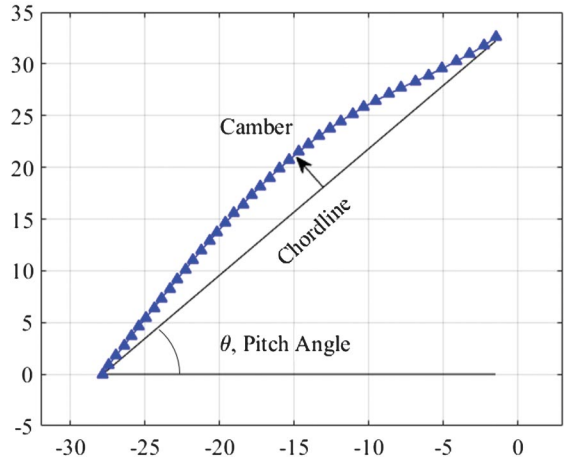

Fig. 16 Pitch and camber definition from cross section at 70% span during midstroke. Scale is millimeters.

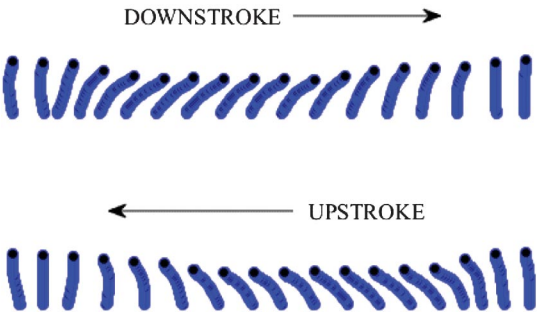

Fig. 17 Wing cross section at 70% span during flap cycle demonstrating variation in pitch and camber.

1. *Pitch Distribution*

As defined in Fig. 16, the geometric pitch angle of the wing at rest (no displacement) is positive 90° and will vary during flapping. The pitch angle at the 60, 70, and 80% spanwise locations during the flap cycle is shown in Fig. 18. Here, the pitch angle is 90° at the stroke ends and is relatively constant at each respective spanwise location from the nondimensional times of 0.1 to 0.3 s and from 0.6 to 0.8 s. This is roughly 40% of the stroke time. Note that the minimum pitch angle varies from 55 to 45° from the 60 to 80% spanwise locations,

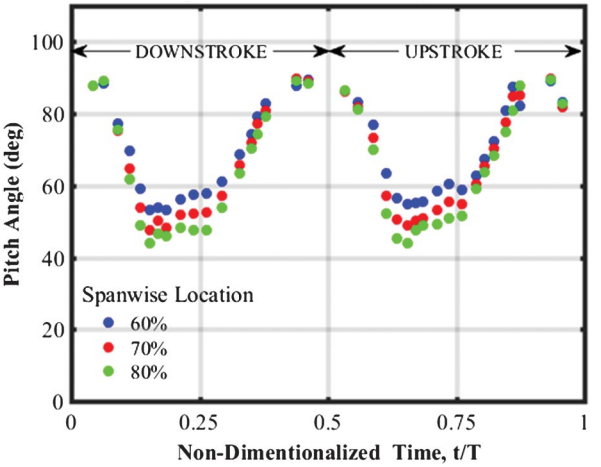

Fig. 18 Wing pitch angle during the flapping cycle at selected spanwise locations.

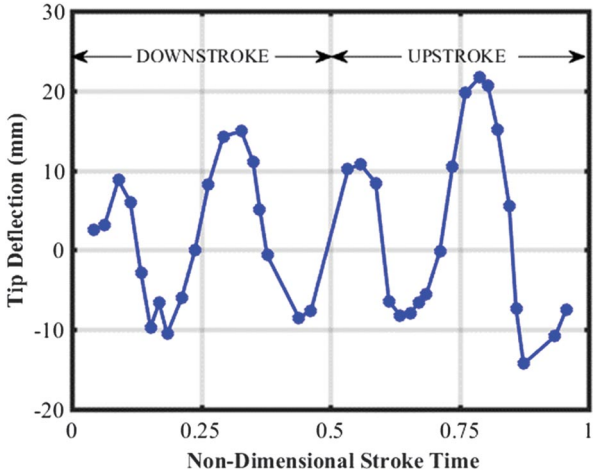

Fig. 19 Wing tip displacement during flapping. Note sinusoidal nature of displacement indicating presence of structural modes.

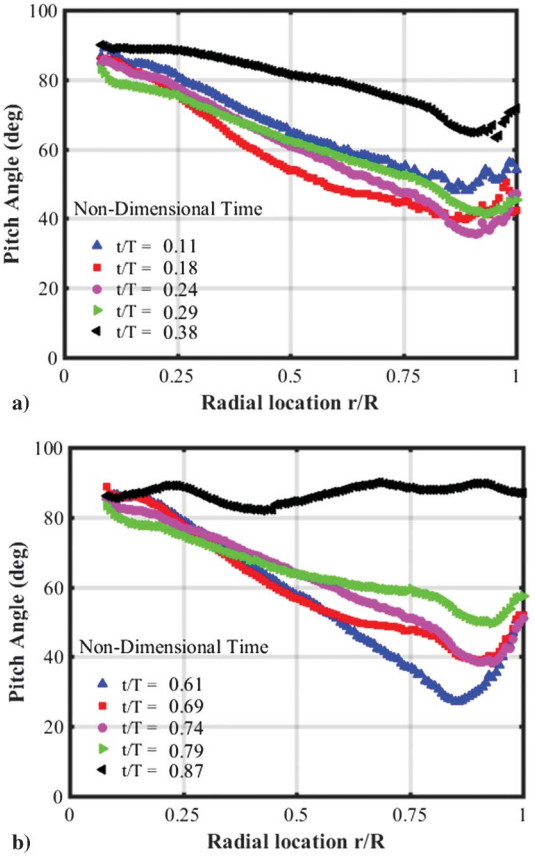

Fig. 20 a) Pitch along wing span during downstroke for selected nondimensional stroke times. b) Pitch along wing span during upstroke for selected nondimensional stroke times.

becoming shallower further away from the root of the wing, indicating significant twist. Note that the wing very quickly twists to the minimum pitch angle ($t/T \approx 0.05$ to 0.15 s, and $t/T \approx 0.55$ to 0.65 s), but more gradually relaxes from there. This could be explained by the fact that the tip of the leading edge spar (plotted in Fig. 19) dips slightly downward during the beginning of the stroke: from $t/T = 0.1$ to $t/T = 0.2$ and again from $t/T = 0.6$ to $t/T = 0.7$. This causes slack in the wing membrane, which allows aerodynamic forces to twist the wing quickly and easily. On the other hand, the leading edge spar bends upward under high aerodynamic loading at the midstroke, pulling the membrane taut, stabilizing the pitch angle, but increasing it slightly. The pitch angle continues to increase after the midstroke and to the end. During this time ($t/T = 0.3$ to $t/T = 0.4$, and from $t/T = 0.8$ to $t/T = 0.9$), the leading edge spar "springs back" to its rest position (Fig. 19). A stiffer leading edge spar would certainly reduce tightening of the membrane slack during high speeds and generate a shallower pitch angle, which may generate more lift. This is entirely plausible, as several flexible wing studies have shown that the stiffer the leading edge spar, the greater the total thrust produced, perhaps for this reason [30,40,45].

In addition to the variation in pitch at discrete spanwise locations during the stroke, the variation in pitch along the span at discrete flap angle times is also important. This is called the rate of twist and is a key parameter in helicopter rotor blade design [59]. Plotted in Figs. 20a (downstroke) and 20b (upstroke) are pitch angles of the wing along its span at specific nondimensional stroke times. These correspond to −40° ($t/T = 0.11$ for downstroke; $t/T = 0.61$ for upstroke), −20° ($t/T = 0.18$ for downstroke; $t/T = 0.69$ for upstroke), 0° (midstroke) ($t/T = 0.24$ for downstroke; $t/T = 0.74$ for upstroke), 20° ($t/T = 0.29$ for downstroke; $t/T = 0.79$ for upstroke), and 40° ($t/T = 0.38$ for downstroke; $t/T = 0.87$ upstroke) flap angles. From this result, it can be seen that the pitch distribution is approximately linear from root to 90% spanwise location, achieving a maximum twist of −60°/wing-length at the midstroke. This is a favorable result because a linear twist distribution is a good approximation of the theoretical hyperbolic twist, which minimizes induced power [59]. How this linear twist varies with flapping is shown in Fig. 21 versus nondimensional stroke time. Here, the maximum twist during downstroke is approximately −75°/wing-length, which is less than during the upstroke, which is −85°/wing-length, which produces a higher peak thrust (Fig. 11). This indicates that greater wing twist improves the lifting generation of the wing. Greater twist means that the tip is at a shallower angle of attack, which may be beneficial in angling the resultant force closer to vertical. This is key, because it has been shown that biological systems with flexible flapping wings are capable of modulating the angle of the resultant force based on wing deflection [60]. Note that asymmetries in twist and measured force are often attributed to asymmetric flapping kinematics. However, this is not the case here

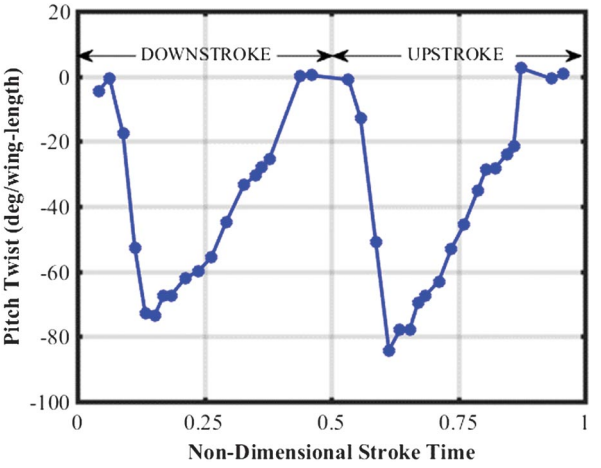

Fig. 21 Pitch twist during flapping. Note dissimilarity in twist between strokes similar to force (Fig 11).

because the kinematics have been carefully tuned to be as symmetric as possible (Fig. 2). Most likely, this phenomenon is due to asymmetries in the wing structure such as gluing the foam membrane or placing the cross spar on only one side of the wing frame. Both of these cause variations between the upstroke and downstroke deflections, and thus the forces normal to the flapping plane.

2. *Camber Distribution*

The camber of the wing, as defined in Fig. 16, can be positive or negative depending on the nature of the flow and structural

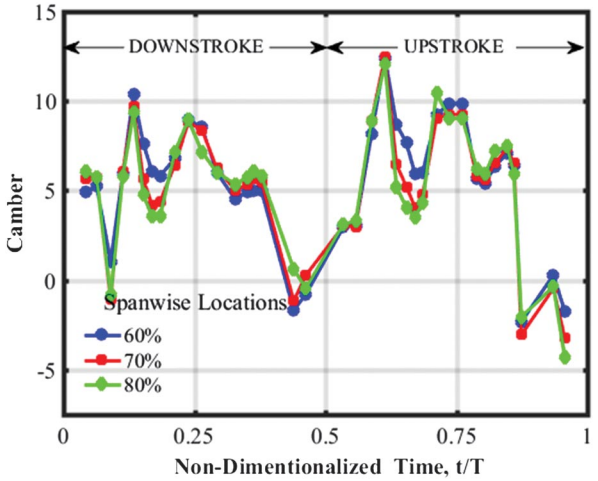

Fig. 22 Wing camber during flapping cycle at selected spanwise locations.

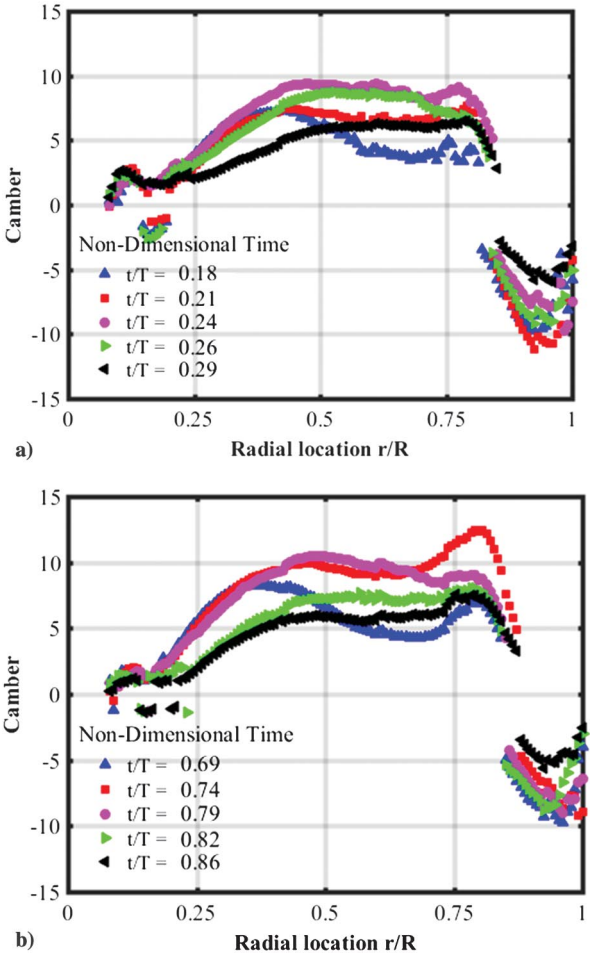

Fig. 23 a) Camber across wing span during downstroke for selected nondimensional times. b) Camber across wing span during upstroke for selected nondimensional times.

deflections. As with the pitch, the cambers at the 60, 70, and 80% spanwise locations are considered here (Fig. 22). The camber peaks at the beginning of the strokes to as high as 12%, rapidly decreases, then rises again, and averages about 7.5% for most of the stroke. Structurally, this can be explained in a similar way as the rapid increase in pitch during the acceleration phase of the wing. The downward bending of the leading edge spar increases the wing slack and allows a greater twist along with camber. However, once the leading edge spar bends upward under high aerodynamic loading, the wing membrane tightens and reduces the camber (refer again to Fig. 19). This type of displacement may help to explain the double peak observed in the forces in Figs. 11 and 15. It has been noted that flexible wings, at least at insect scales, can provide increases in lift due to the cambering effect of the wing during flapping; hence, wing camber is expected to significantly affect lift [60]. Thus the current flexible flapping wing may benefit from structural design improvements that provide better camber control with fewer sharp peaks.

As with pitch, the spanwise distribution of camber at discrete flap times is also of interest and is plotted in Fig. 23a (downstroke) and Fig. 23b (downstroke) at selected nondimensional stroke times. There is a relatively constant 10% camber along much of the span, except for from the 85% span location to the tip, at which the camber is negative. This is likely because this spanwise location is beyond the end of the diagonal cross spar, which is responsible for providing wing camber (Fig. 16). One solution to this problem may be to either extend the present cross spar, or add an additional cross spar positioned at a shallower angle relative to the leading edge such that it extends further along the span horizontally. Such efforts are of interest because the outboard regions of the wing are traveling at the highest tangential velocity, and thus generating significant thrust. Therefore, proper camber and pitch angle are of utmost importance at these locations.

B. Flowfield Characteristics

The flowfield measurements from the spanwise PIV experiments were aimed at investigating detailed flowfield structures in the immediate vicinity of the wing surface. Knowledge of these may help explain the force production on the wing as well as shed light on how structural deflections affect the aerodynamics. The PIV experiments resolved the flowfield at the 70% spanwise location at discrete azimuthal locations. These results are plotted in Figs. 24a–24l, in which the dark arrows indicate velocity magnitude and direction in the inertial frame, and the color contours indicate vorticity.

There are a few key features to note. First, the wing starting vortex, seen most clearly in the first four images, qualitatively demonstrates that the flow satisfies Kelvin's circulation theorem. The tail of the starting vortex grows longer and extends downward as the wing progresses forward in the stroke. Second, during the acceleration phase of the wing, the leading edge bubble begins to form (Figs. 24a–24f). As the speed of the wing increases, the pitch angle decreases to its midstroke value (approximately 45° at the 70% spanwise location). One would expect separated flow at such steep pitch angles from deep stall effects on a cambered airfoil in steady flow. However, due to the highly unsteady nature of the flow under investigation and dynamic stall effects, the flow quite clearly remains attached all the way to the midstroke (Fig. 24g). The smooth and gradual development of the leading edge bubble seems to indicate that the double peak observed in the lift force is the result of wing deflection rather than substantial changes in flowfield features (Figs. 11 and 25). Third, during the deceleration phase of the wing, the leading edge vortex fully matures from the attached flow on the wing leading edge. It begins to take shape as the wing reaches the midstroke position and continues to grow larger until bursting about 20° before the stroke end (Fig. 24j). Interestingly, the vortex develops until its diameter is approximately equal to the chord of the wing at the 70% location. Such phenomenon is favorable in generating lift, because the magnitude of the aerodynamic force is proportional to the size of the leading edge vortex on flapping wings [61]. Additionally, the instant at which the leading edge vortex bursts (Fig. 24j) may also help to explain the quick return of the leading edge spar from maximum displacement at midstroke down to its undeformed configuration (Fig. 20, from $t/T = 0.3$ to $t/T = 0.4$), because this is the time at which the wing becomes unloaded in lift.

Finally, there is the trailing edge vortex, which is formed as the wing begins to decelerate and follows a similar development and shedding pattern as the leading edge vortex. Because of the leading edge spar and thus the entire wing moving downward after being deflected upward during maximum loading, the trailing edge vortex

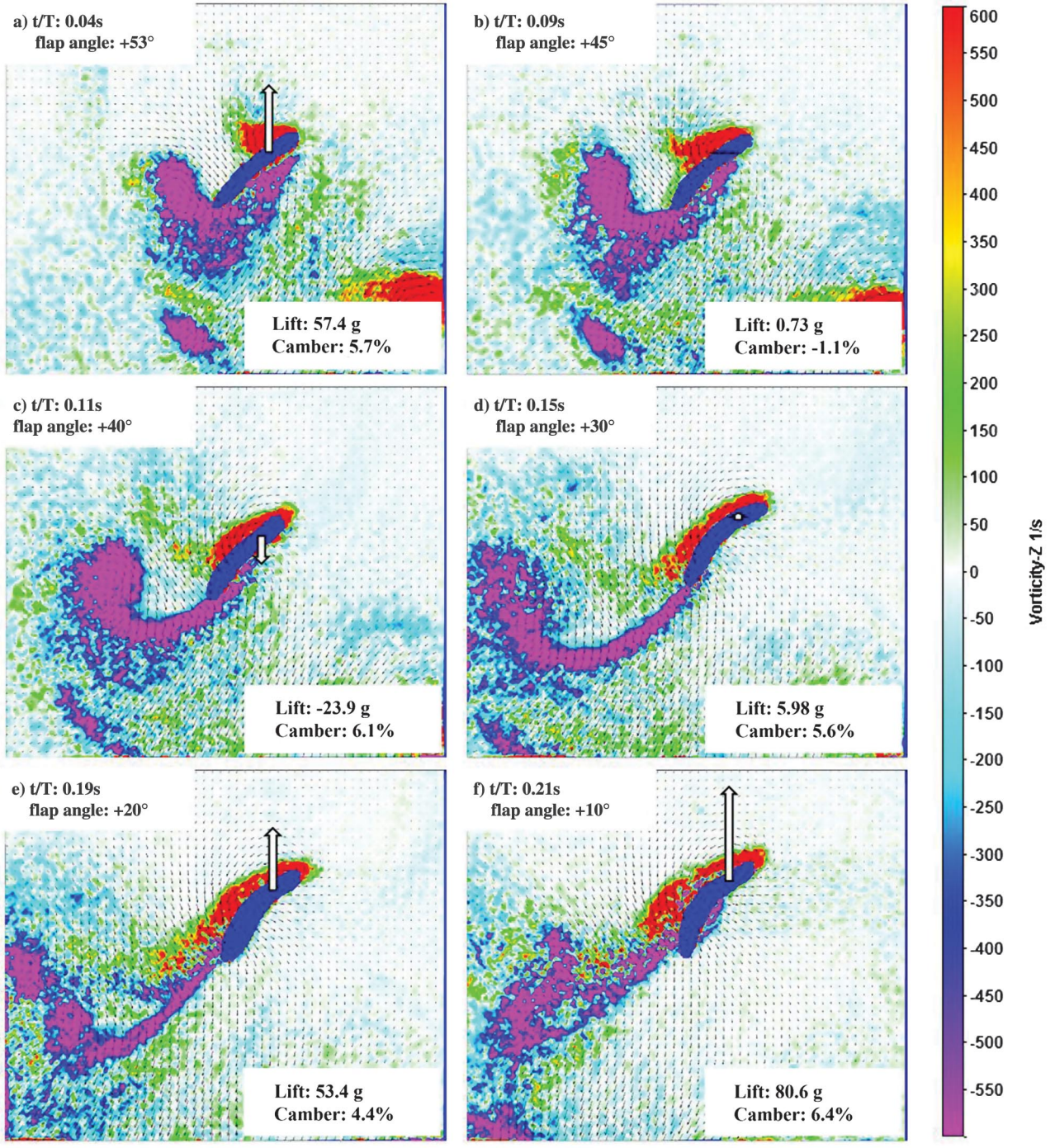

Fig. 24 a–l) Chordwise PIV measurements. Flowfield direction is indicated by arrows, and vorticity by color contour.

appears to move upward slightly relative to the wing. But this is due to the wing itself moving downward as it relaxes after unloading. There is also significant leading and trailing edge vortex interaction as seen in Figs. 24h–24l. This indicates that assuming these to be independent phenomena in aerodynamic simulations may not be valid. Also, there are no significant interactions with previously shed wakes, though this needs to be investigated further in a more detailed study.

The second PIV experiments investigated the development of the leading and trailing edge vortices along the wing span at the 30, 50, and 70% spanwise locations, and at three selected flap angles (nondimensional stroke times). These were $+30°$ ($t/T = 0.15$ s), $0°$ ($t/T = 0.24$ s), and $-30°$ ($t/T = 0.35$ s). The nine PIV measurement plots are shown in Fig. 25 with velocity arrows and vorticity color contours in the background as before. At the innermost locations (30 and 50%), the flow is separating slightly from the wing at $t/T = 0.15$ s, which could be due to the extremely high inboard angles of attack (Figs. 25a and 25d). Further out on the wing (70% location), the flow is attached even though the wing is traveling at a higher speed (Fig. 25g). This may help to explain why the introduction of a flexible joint between the wing root and root spar was so effective in increasing the coefficient of lift of the wing. The flexible shim allows the root to bend relative to the vertical position, decreasing the angle of attack slightly, and preventing full separation of the flow (see Ref. [17] for more details). At the midstroke ($t/T = 0.24$ s) the leading edge vortex has fully formed and is both stable and attached along the entire span, simply growing larger conically along the span (Figs. 25b, 25e, and 25h). At $t/T = 0.35$ s, the size difference along the span is even more dramatic (Figs. 25c, 25f, and 25i). The variation in vortex diameter along the span could be due to a velocity effect, and no doubt will influence the lift distribution along the wing span, which must be investigated in more

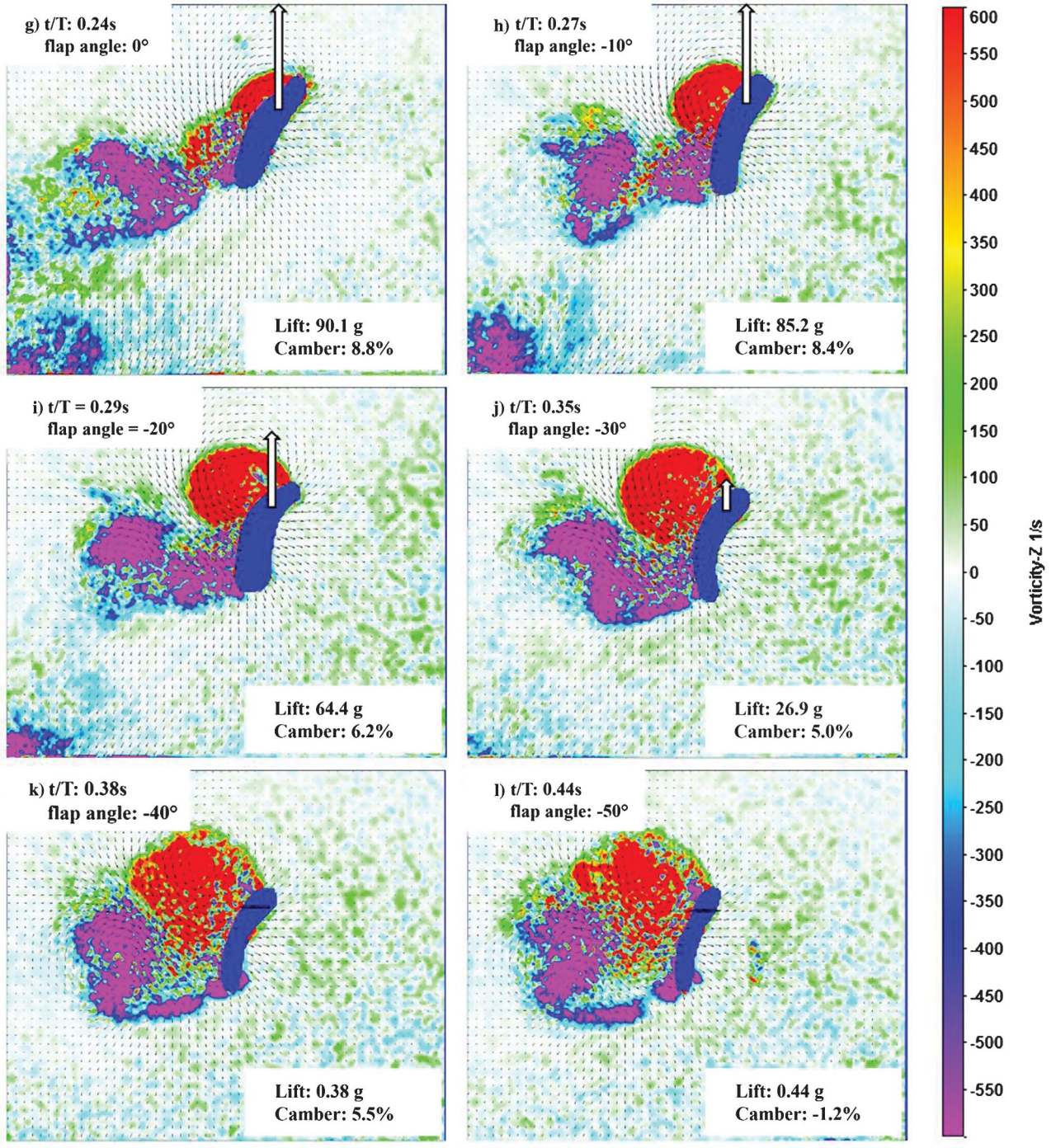

Fig. 24 Continued.

detail. Concerning the development and shedding of the trailing edge vortex, at $t/T = 0.15$ s, the trailing edge flow is dominated by the starting vortex (Figs. 25a, 25d, and 25g), which persists at the 30 and 50% locations at the midstroke (Figs. 25b and 25e) and at $t/T = 0.35$ s (Figs. 25c and 25f). However, a new trailing edge vortex starts to form at the 70% midstroke position (Fig. 25h) and grows slightly, but quickly disperses afterward (Fig. 25i). As noted previously, there is significant leading and trailing edge vortex interaction at the 70% spanwise location. Because of the increase in wing chord and decrease in vortex diameter, this phenomenon does not occur at any locations further inboard.

C. Deflection and Flowfield Relations

This study has resulted in a significant amount of experimental results quantifying the physical process of force generation on a flexible flapping wing. Because force, deflection, and flowfield are so closely intertwined, it is desirable to establish basic relationships among them. To do this, the reciprocating motion of the flapping wing can be related to the continuous rotation of a traditional helicopter rotor blade by applying blade element theory (BET), a technique often employed to characterize the aerodynamics of rotor blades. According to this theory, the aerodynamics of a rectangular twisted rotor blade can be quantified in terms of an equivalent untwisted blade with the same pitch angle as the twisted rotor blade at the 75% radial location [57]. Using the same mathematical technique, but for a flapping wing with a planform shape and aspect ratio used for this robotic hummingbird, the equivalent radial location is approximately 70%. At this location the pitch angle varies according to Fig. 18 during the flap cycle. Thus the flowfield measurements at the 70% spanwise location are of most interest, which is what was

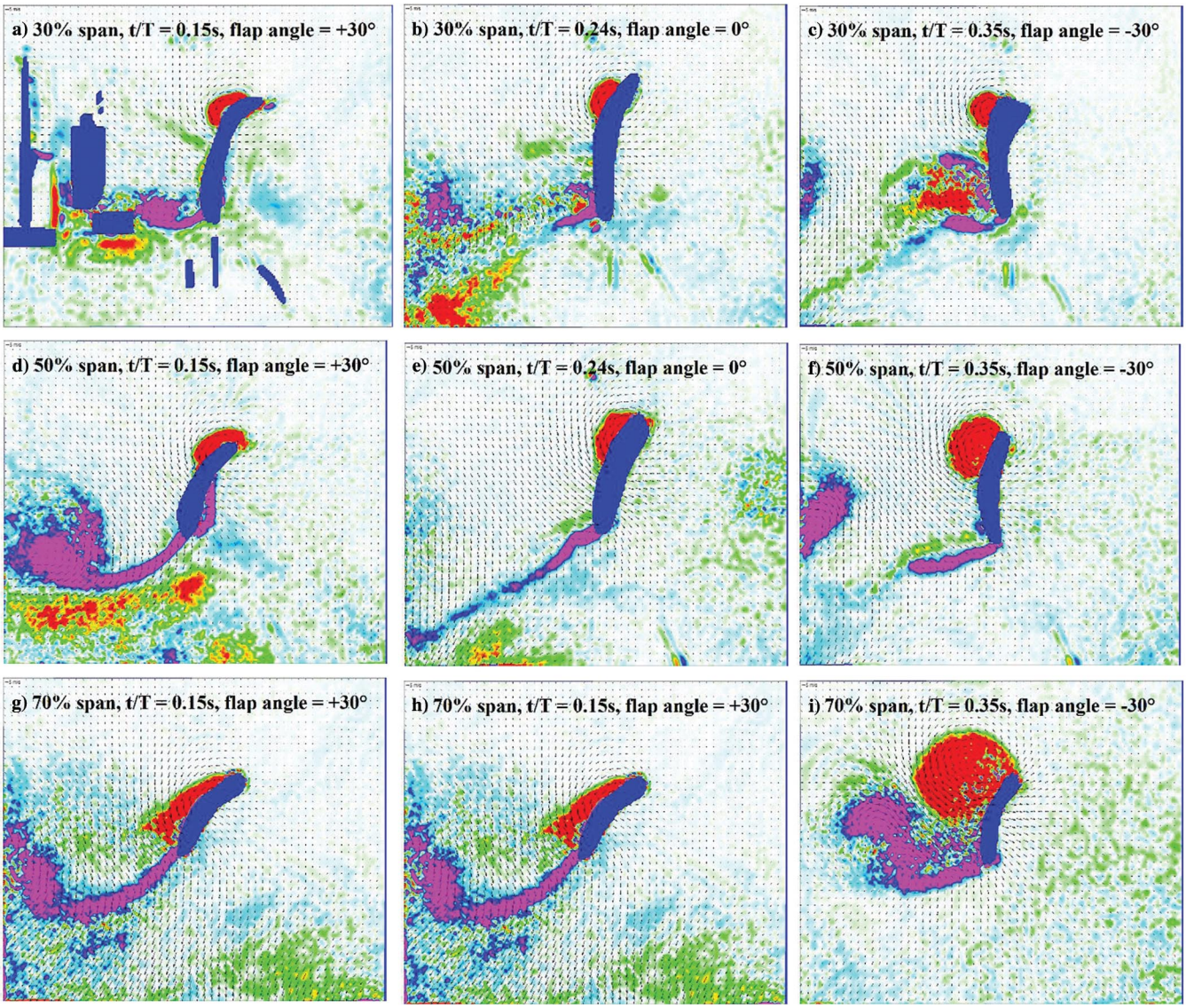

Fig. 25 Chordwise PIV measurements at selected spanwise locations, 30, 50, and 70%.

investigated and shown in Figs. 24a–24l with the instantaneous force and camber measurements included on each chart. Camber and unsteady aerodynamics alternated affecting the lift production of the wing. Using these two measured quantities in conjunction with flowfield, some observations relating wing shape and aerodynamics can be made.

First, note the drop in lift at a nondimensional stroke time of $t/T = 0.09$ s shortly after the start of the downstroke motion. It is unlikely that the drop in lift is associated with unsteady aerodynamics, because there is relatively little qualitative change between the flowfield features at $t/T = 0.09$ s and $t/T = 0.04$ s except for further growth of the starting vortex. Additionally, Figs. 24a and 24b show fully attached flow during this time. On the other hand, the camber of the wing at the 70% spanwise location is −1.1%, the most likely explanation for the sharp decrease in lift. As discussed above, this could be prevented by a more controlled camber development. Examining the deflection field shows some relaxation of the wing membrane at this point due to downward deflection of the leading edge spar. This removes tautness of the wing membrane, introduces wrinkles, and creates irregular cross-sectional shapes in the fabric. This demonstrates that even with the aid of lift-enhancing unsteady aerodynamic phenomena (delayed stall), if wing shape is not properly maintained, lift can be lost. This gives experimental validation to the postulate that biological creatures do not rely solely on low-Reynolds-number unsteady aerodynamics, but also on a properly tuned wing structure for generating large force coefficients.

Second, observe also the lift and camber trends from $t/T = 0.19$ s to $t/T = 0.29$ s, corresponding to approximately 40° of wing flapping (Fig. 24). Here, the velocity has a significant effect on the lift produced because it increases to its maximum at the midstroke, generating a force of 90 g, equal to one and a half times the robotic hummingbird weight. The camber increases to a maximum during this time, which contributes to a spike in lift generation, and then smoothly decreases afterward. Because the camber of the wing generally follows the velocity trend, it is likely that aerodynamic forces are the key player in shaping the wing during this time. Additionally, note that the strong leading edge vortex develops at this time, which, in combination with the high wing speed, generates a smoother wing shape and more camber. The end result of this effect is to increase the lift.

Finally, during the deceleration phase of the stroke from $t/T = 0.29$ s to $t/T = 0.38$ s, the leading edge vortex grows to its maximum and bursts. At this time the camber is relatively constant, and changes by no more than 20% as it varies between 6.2 and 5.0%. On the other hand, the lift drops by 99.4% from 64.4 g force to 0.38 g. The velocity does not vary this significantly over 20 degrees of rotation and thus cannot adequately explain this phenomenon. The only explanation for the massive decrease in lift is the bursting of the

strong leading edge vortex that has developed to have a diameter approximately as large as the chord. After bursting, it quickly dissipates during this portion of the flap cycle, and any large low-pressure regions on the wing are lost in a relatively short period of time. Here, the wing shape is quite conducive to lift generation (moderate pitch angle and positive camber), but the unsteady aerodynamics have a strong negative effect and destroy the lift on the wing. This is the inverse of the above observation in which the negative wing camber canceled the positive influence of attached flow at high angles of attack.

IV. Conclusions

This study marks an important endeavor to quantify the aeromechanical elements of a flapping flexible wing used on a two-winged robotic hummingbird in hover. The aerostructural interactions were characterized by measuring instantaneous forces normal to the flapping plane, wing deflections, and flowfield during the flapping cycle. The purpose of such an in-depth investigation of this particular flexible flapping wing design is to further our understanding of the physics of hummingbird flight and garner key insights into designing flexible flapping wings for hover-capable flapping wing MAVs. Some of the key results are summarized below.

1) Inertial force calculation via displacement measurements was used successfully to calculate pure instantaneous aerodynamic lift. This study has developed and proven this technique for the first time and applied it to a hovering flapping flexible wing. The procedure for calculating inertial loads from time-varying displacements has been tabulated carefully, and is general enough to be used on any flexible structure with known mass distribution.

2) Pitch distributions for the flexible flapping wing have been extracted from DIC measurements and have shown a linear twist rate of $-60°/$length near the midstroke. Additionally, it has been found that the wing twists to a greater degree during the upstroke, which also produces higher levels of thrust even though the kinematics are symmetric. This is most likely due to an asymmetry in the wing structure, which allows greater compliancy in one direction.

3) Camber as a function of flap angle has also been quantified, and is found to experience large variations during the flapping stroke, contributing to twin lift peaks during each stroke. Such behavior of the wing structure can negatively affect lift production, and should be designed to moderate, but not constrain, the motion of the flexible membrane.

4) Pitch as a function of flap angle has been quantified at the 60, 70, and 80% locations. At these locations, the minimum pitch angle varies from 55° to 45°, and it has been observed that the wing rapidly twists up but gradually relaxes starting about midstroke. The excessive amplitude of vertical bending of the leading edge spar contributes to this behavior. Thus a stiffer leading edge spar would likely result in more favorable wing pitching throughout the stroke.

5) Chordwise PIV measurements at the 70% span location have captured key flowfield features during the downstroke in the immediate vicinity of the wing. The presence of a strong starting vortex was observed. Additionally, attached flow was recorded during the acceleration phase of the wing, although the angle of attack was very large, indicating the presence of dynamic stall. Then, during the deceleration phase, the leading edge vortex developed extensively until its diameter was approximately equal to the chord at the 70% location. There is substantial interaction observed between the leading and trailing edge vortices, indicating that each cannot be treated as an independent phenomenon. As the wing nears the stroke end, both the leading and trailing edge vortices burst.

6) Additional chordwise PIV measurements of the flowfield were also conducted at 30 and 50% spanwise locations to characterize the development of vortices along the span. For locations far inboard at 30% span, the flow experienced some separation before the midstroke due to the excessively high angles of attack. The growth of the leading edge vortex along the span was roughly conical in nature.

7) Wing camber, pitch angle, and unsteady aerodynamics are equally important to the positive force production of a flexible flapping wing, especially at midstroke during highest wing velocity. A camber of around 8% and pitch angle of ∼50° at the 70% location are capable of generating instantaneous lift three times larger than the mean lift during the entire flap stroke.

The data generated from this study have led to the characterization of the aeromechanics of a flapping flexible wing used on a hover-capable robotic hummingbird by quantifying the relationship between wing shape, lift, and aerodynamics. These results mark a key point in quantifying these relationships at a fundamental level, because wing design hinges heavily on the coupling between these to generate lift. It is hoped that the results of this study will enable more efficient and systematic development of flexible, flapping wings for biologically inspired flying platforms, as well as permit the experimental validation of high-fidelity computational design tools.

Acknowledgment

This work was supported through internal funding from Texas A&M University.

References

[1] Gill, F., and Donsker, D., (eds.), *IOC World Bird List (v 7.1)*, 2017, http://www.worldbirdnames.org/.

[2] Sabrosky, C. W., "How Many Insects Are There?" *Insects: The Yearbook of Agriculture*, U.S. Dept. of Agriculture, Washington, D. C., 1952, Chap. 1.

[3] Tudge, C., *The Variety of Life*, Oxford Univ. Press, Oxford, 2000, Chap. 10.

[4] Mazaheri, K., and Ebrahimi, A., "Experimental Investigation of the Effect of Chordwise Flexibility on the Aerodynamics of Flapping Wings in Hovering Flight," *Journal of Fluids and Structures*, Vol. 26, No. 4, 2010, pp. 544–558. doi:10.1016/j.jfluidstructs.2010.03.004

[5] Jensen, M., and Weis-Fogh, T., "Biology and Physics of Locust Flight V. Strength and Elasticity of Locust Cuticle," *Philisophical Transactions of the Royal Society*, Vol. B245, No. 721, 1962, pp. 137–169. doi:10.1098/rstb.1962.0008

[6] Rees, C. J. C., "Aerodynamic Properties of an Insect Wing Section and a Smooth Aerofoil Compared," *Nature*, Vol. 258, No. 5531, Nov. 1975, pp. 141–142. doi:10.1038/258141a0

[7] Wootton, R. J., "Leading Edge Section and Asymmetric Twisting in the Wings of Flying Butterflies (Insecta, Papilionoidea)," *Journal of Experimental Biology*, Vol. 180, 1993, pp. 105–117.

[8] Wootton, R. J., Herbert, R. C., Young, P. G., and Evans, K. E., "Approaches to the Structural Modelling of Insect Wings," *Philosophical Transactions of the Royal Society London*, Vol. B358, No. 1437, 2003, pp. 1577–1587. doi:10.1098/rstb.2003.1351

[9] Walker, S. M., Thomas, A. L. R., and Taylor, G. K., "Photogrammetric Reconstruction of High-Resolution Surface Topographies and Deformable Wing Kinematics of Tethered Locusts and Free-Flying Hoverflies," *Journal of the Royal Society Interface*, Vol. 6, No. 33, 2009, pp. 351–366. doi:10.1098/rsif.2008.0245

[10] Dalton, S., *Borne on the Wind: The Extraordinary World of Insects in Flight*, Reader's Digest Press, New York, 1975, Chap. 1.

[11] Wootton, R. J., The Mechanical Design of Insect Wings, *Scientific American*, Vol. 263, No. 5, Nov. 1990, pp. 114–120.

[12] Willmott, A. P., and Ellington, C. P., "The Mechanics of Flight in the Hawkmoth Manduca Sexta. I. Kinematics of Hovering and Forward Flight," *Journal of Experimental Biology*, Vol. 200, No. 21, 1997, pp. 2705–2722.

[13] Ennos, A. R., "The Inertial Cause of Wing Rotation in Diptera," *Journal of Experimental Biology*, Vol. 140, No. 1, 1988, pp. 161–169.

[14] Bergou, A. J., Xu, S., and Wang, Z. J., "Passive Wing Pitch Reversal in Insect Flight," *Journal of Fluid Mechanics*, Vol. 591, 2007, pp. 321–337. doi:10.1017/S0022112007008440

[15] Kang, C., and Shyy, W., "Passive Wing Rotation in Flexible Flapping Wing Aerodynamics," *Proceedings of the 30th AIAA Applied Aerodynamics Conference*, AIAA Paper 2012-2763, June 2012.

[16] Song, J., Luo, H., and Hedrick, T. L., "Wing-Pitching Mechanism of Hovering Ruby-Throated Hummingbird," *Bioinspiration and Biomimetics*, Vol. 10, No. 1, 2015, Paper 016007. doi:10.1088/1748-3190/10/1/016007

[17] Coleman, D., Benedict, M., Hrishikeshavan, V., and Chopra, I., "Development of a Robotic Hummingbird Capable of Controlled Hover," *AHS Journal*, Vol. 62, No. 3, 2017, pp. 1–9. doi:10.4050/JAHS.62.032003

[18] Keennon, M., Klingebiel, K., Won, H., and Andriukov, A., "Development of the Nano Hummingbird: A Tailless Flapping Wing Micro Air Vehicle," *50th AIAA Aerospace Sciences Meeting*, AIAA Paper 2012-0588, Jan. 2012.

[19] Phan, H. V., and Park, H. C., "Remotely Controlled Flight of an Insect-Like Tailless Flapping-Wing Micro Air Vehicle," *Proceedings of the 12th International Conference on Ubiquitous Robots and Ambient Intelligence (URAI 2015)*, KINTEX, Goyang City, South Korea, Oct. 2015, pp. 315–317.

[20] Karasek, M., "Robotic Hummingbird: Design of a Control Mechanism for a Hovering Flapping Wing Micro Air Vehicle," Ph.D. Thesis, Universite Libre De Bruxelles, 2014.

[21] Combes, S. A., and Daniel, T. L., "Into Thin Air: Contributions of Aerodynamic and Inertial-Elastic Forces to Wing Bending in the Hawkmoth Manduca Sexta," *Journal of Experimental Biology*, Vol. 206, No. 17, 2003, pp. 2999–3006. doi:10.1242/jeb.00502

[22] Daniel, T., and Combes, S., "Flexing Wings and Fins: Bending by Inertial or Fluid Dynamic Forces?" *Integrative and Comparative Biology*, Vol. 42, No. 5, 2002, pp. 1044–1049. doi:10.1093/icb/42.5.1044

[23] Combes, S. A., and Daniel, T. L., "Flexural Stiffness in Insect Wings I. Scaling and Influence of Wing Venation," *Journal of Experimental Biology*, Vol. 206, No. 17, 2003, pp. 2979–2987. doi:10.1242/jeb.00523

[24] Combes, S. A., and Daniel, T. L., "Flexural Stiffness in Insect Wings II. Spatial Distribution and Dynamic Wing Bending," *Journal of Experimental Biology*, Vol. 206, No. 17, 2003, pp. 2989–2997. doi:10.1242/jeb.00524

[25] Kruyt, J. W., Quicazán-Rubio, E. M., van Heijst, G. H., Altshuler, D. L., and Lentink, D., "Hummingbird Wing Efficacy Depends on Aspect Ratio and Compares with Helicopter Rotors," *Journal of the Royal Society Interface*, Vol. 11, No. 99, 2014, pp. 1–12. doi:10.1098/rsif.2014.0585

[26] Warrick, D. R., Tobalske, B. W., and Powers, D. R., "Lift Production in the Hovering Hummingbird," *Proceedings of the Royal Society B*, Vol. 276, No. 1674, 2009, pp. 3747–3752. doi:10.1098/rspb.2009.1003

[27] Zhao, L., Huang, Q., Deng, X., and Sane, S. P., "Aerodynamic Effects of Flexibility in Flapping Wings," *Journal of the Royal Society Interface*, Vol. 7, No. 44, 2010, pp. 485–497. doi:10.1098/rsif.2009.0200

[28] Maybury, W. J., and Lehmann, F., "The Fluid Dynamics of Flight Control by Kinematic Phase Lag Variation Between Two Robotic Insect Wings," *Journal of Experimental Biology*, Vol. 207, No. 26, 2004, pp. 4707–4726. doi:10.1242/jeb.01319

[29] Truong, Q. T., Phan, H. V., Park, H. C., and Koh, J. H., "Effect of Wing Twisting on Aerodynamic Performance of Flapping Wing System," *AIAA Journal*, Vol. 51, No. 7, 2013, pp. 1612–1620. doi:10.2514/1.J051831

[30] Ho, S., Nassef, H., Pornsinsirirak, N., Tai, Y., and Ho, C., "Unsteady Aerodynamics and Flow Control for Flapping Wing Flyers," *Progress in Aerospace Sciences*, Vol. 39, No. 8, 2003, pp. 635–681. doi:10.1016/j.paerosci.2003.04.001

[31] Colmenares, D., Kania, D., Zhang, W., and Sitti, M., "Compliant Wing Design for a Flapping Wing Micro Air Vehicle," *IEEE International Conference on Intelligent Robots and Systems*, IEEE Publ., Piscataway, NJ, 2015, pp. 32–39.

[32] Wu, P., Stanford, B. K., Sallstrom, E., Ukeiley, L., and Ifju, P. G., "Structural Dynamics and Aerodynamics Measurements of Biologically Inspired Flexible Flapping Wings," *Bioinspiration and Biomimetics*, Vol. 6, No. 1, 2011, Paper 016009. doi:10.1088/1748-3182/6/1/016009

[33] Sallstrom, E., and Ukeiley, L., "Flow Measurements in the Wake of Flexible Flapping Wings," *Proceedings of the 28th AIAA Applied Aerodynamics Conference*, AIAA Paper 2010-4945, June–July 2010.

[34] Banerjee, A., Ghosh, S. K., and Das, D., "Aerodynamics of Flapping Wing at Low Reynolds Numbers: Force Measurement and Flow Visualization," *International Scholarly Research Network, ISRN Mechanical Engineering*, Vol. 2011, 2011, Paper 162687. doi:10.5402/2011/162687

[35] Singh, B., and Chopra, I., "Insect-Based Hover-Capable Flapping Wings for Micro Air Vehicles: Experiments and Analysis," *AIAA Journal*, Vol. 46, No. 9, Sept. 2008, pp. 2115–2135. doi:10.2514/1.28192

[36] Maglasang, J., Isogai, K., and Goto, N., "Aerodynamic Study and Mechanization Concept for Flapping-Wing Micro Aerial Vehicles," *Memoirs of the Faculty of Engineering, Kyushu University*, Vol. 66, No. 1, 2006, pp. 71–82.

[37] Smith, M. J. C., "Simulating Moth Wing Aerodynamics: Towards the Development of Flapping-Wing Technology," *AIAA Journal*, Vol. 34, No. 7, 1996, pp. 1348–1355. doi:10.2514/3.13239

[38] Chaudhuri, A., Haftka, R. T., Ifju, P., Chang, K., Tyler, C., and Schmitz, T., "Experimental Flapping Wing Optimization and Uncertainty Quantification Using Limited Samples," *Structural and Multidisciplinary Optimization*, Vol. 51, No. 4, 2015, pp. 957–970. doi:10.1007/s00158-014-1184-x

[39] Ren, H., Wu, Y., Huang, P. G., and Evans, J., "PIV Study of Flow Fields in the Near-Wake Region of a Flapping Wing Micro Air Vehicle," *Proceedings of the 49th AIAA Aerospace Sciences Meeting Including the New Horizons Forum and Aerospace Exposition*, AIAA Paper 2011-571, Jan. 2011.

[40] Nan, Y., Karasek, M., Lalami, M. E., and Preumont, A., "Experimental Optimization of Wing Shape for a Hummingbird-Like Flapping Wing Micro Air Vehicle," *Bioinspiration and Biomimetics*, Vol. 12, No. 2, 2017, Paper 026010. doi:10.1088/1748-3190/aa5c9e

[41] Ames, R. G., "On the Flowfield and Forces Generated by a Rectangular Wing Undergoing Moderate Reduced Frequency Flapping at Low Reynolds Number," Ph.D. Thesis, Georgia Inst. of Technology, 2009.

[42] Ellington, C. P., "The Aerodynamics of Hovering Insect Flight. Part VI: Lift and Power Requirements," *Philosophical Transactions of the Royal Society of London. Series B*, Vol. 305, No. 1122, 1984, pp. 145–181. doi:10.1098/rstb.1984.0054

[43] Lehmann, F.-O., and Dickinson, M. H., "The Changes in Power Requirements and Muscle Efficiency During Elevated Force Production in the Fruit Fly Drosophila Melanogaster," *Journal of Experimental Biology*, Vol. 200, No. 7, 1997, pp. 1133–1143.

[44] Sun, M., and Tang, J., "Lift and Power Requirements of Hovering Flight in Drosophila virilis," *Journal of Experimental Biology*, Vol. 205, No. 16, 2002, pp. 2413–2427.

[45] Wu, P., Ifju, P., and Stanford, B., "Flapping Wing Structural Deformation and Thrust Correlation Study with Flexible Membrane Wings," *AIAA Journal*, Vol. 48, No. 9, Sept. 2010, pp. 2111–2122. doi:10.2514/1.J050310

[46] Tran, J., Sirohi, J., Gao, H., and Wei, M., "Reduced Order Modeling of Loads and Deformation of a Flexible Flapping Wing," *AIAA 56th AIAA/ASCE/AHS/ASC Structures, Structural Dynamics, and Materials Conference*, AIAA Paper 2015-0177, 2015.

[47] Simons, E. L. R., Hieronymus, T. L., and O'Connor, P. M., "Cross Sectional Geometry of the Forelimb Skeleton and Flight Mode in Pelecaniform Birds," *Journal of Morphology*, Vol. 272, No. 8, 2011, pp. 958–971. doi:10.1002/jmor.v272.8

[48] Ennos, A. R., "The Importance of Torsion in the Design of Insect Wings," *Journal of Experimental Biology*, Vol. 140, No. 1, 1988, pp. 137–160.

[49] Weis-Fogh, T., "Quick Estimates of Flight Fitness in Hovering Animals, Including Novel Mechanisms for Lift Production," *Journal of Experimental Biology*, Vol. 59, No. 1, 1973, pp. 169–230.

[50] Lehmann, F. O., Sane, S. P., and Dickinson, M., "The Aerodynamic Effects of Wing–Wing Interaction in Flapping Insect Wings," *Journal of Experimental Biology*, Vol. 208, No. 16, 2005, pp. 3075–3092. doi:10.1242/jeb.01744

[51] Ring, A. V., Product-Manual for DaVis 8.2, *StrainMaster DaVis 8.4*, LaVision GmbH, Gottingen Germany, Jan. 2017.

[52] Groen, M. A., "PIV and Force Measurements on the Flapping-Wing MAV DelFly II: An Aerodynamic and Aeroelastic Investigation into Vortex Development," Master of Science Thesis, Delft Univ. of Technology, Delft, The Netherlands, 2010.

[53] Benedict, M., Coleman, D., Mayo, D. B., and Chopra, I., "Experiments on Rigid Wing Undergoing Hover-Capable Flapping Kinematics at Micro-Air-Vehicle-Scale Reynolds Numbers," *AIAA Journal*, Vol. 54, No. 4, 2016, pp. 1145–1157. doi:10.2514/1.J052947

[54] Percin, M., Hu, Y., van Oudheusden, B. W., Remes, B., and Scarano, F., "Wing Flexibility Effects Clap and Fling," *International Journal of Micro Air Vehicles*, Vol. 3, No. 4,2011, pp. 217–227.

[55] Ramasamy, M., and Leishman, J. G., "Phase-Locked Particle Image Velocimetry Measurements of a Flapping Wing," *Journal of Aircraft*, Vol. 43, No. 6, Nov.–Dec. 2006, pp. 1867–1875. doi:10.2514/1.21347

[56] Warrick, D. R., Tobalske, B. W., and Powers, D. R., "Aerodynamics of the Hovering Hummingbird," *Nature*, Vol. 435, No. 7045, June 2005, pp. 1094–1097. doi:10.1038/nature03647

[57] Altshuler, D. L., Princevac, M., Pan, H., and Lozano, J., "Wake Patterns of the Wings and Tail of Hovering Hummingbirds," *Journal of Experimental Fluids*, Vol. 46, No. 5, 2009, pp. 835–846. doi:10.1007/s00348-008-0602-5

[58] Benedict, M., Deflections on a Flexible Robotic Hummingbird Wing at 20 Hz, July 2017, https://www.youtube.com/watch?v=HvwJQY8Clbk.

[59] Leishman, J. G., *Principles of Helicopter Aerodynamics*, Cambridge Univ. Press, New York, 2000.

[60] Ennos, A. R., "Functional Wing Morphology and Aerodynamics of Panorpa Germanica (Insecta: Mecoptera)," *Journal of Experimental Biology*, Vol. 143, No. 1, 1989, pp. 267–284.

[61] Ellington, C. P., Vandenberg, C., Willmott, A. P., and Thomas, A. L. R., "Leading-Edge Vortices in Insect Flight," *Nature*, Vol. 384, No. 6610, 1996, pp. 626–630. doi:10.1038/384626a0